The Astrophysical Journal, 732:15 (8pp), 2011 May 1 doi:10.1088/0004-637X/732/1/15

ESTIMATION OF THE RECONNECTION ELECTRIC FIELD IN THE 2003 OCTOBER 29 X10 FLARE

Ya-Hui Yang[1], C. Z. Cheng[1,2,3], Säm Krucker[4,5], and Min-Shiu Hsieh[2,6]
[1] Plasma and Space Science Center, National Cheng Kung University, Tainan 70101, Taiwan;
yhyang@pssc.ncku.edu.tw, frankcheng@pssc.ncku.edu.tw
[2] Institute of Space, Astrophysical and Plasma Sciences, National Cheng Kung University, Tainan 70101, Taiwan; mhsieh2@alaska.edu
[3] School of Space Research, Kyung Hee University, Republic of Korea
[4] Space Sciences Laboratory, University of California, Berkeley, CA 94720–7450, USA; krucker@ssl.berkeley.edu
[5] Institute of 4D Technologies, School of Engineering, University of Applied Sciences North Western Switzerland, Windisch, Switzerland
Received 2010 November 8; accepted 2011 February 22; published 2011 April 8

ABSTRACT

The electric field in the reconnecting current sheet of the 2003 October 29 X10 flare is estimated to be a few kV m^{-1} in this study, based on the rate of change in the photospheric magnetic flux in the newly brightened areas of *Transition Region and Coronal Explorer* (*TRACE*) UV ribbons. For comparison, the motion speed of *Reuven Ramaty High Energy Solar Spectroscopic Imager* (*RHESSI*) hard X-ray (HXR) footpoints and the photospheric magnetic field strength are also used for the electric field calculation. This X10 flare event is selected due to its distinct two-phase HXR kernel motion, two arcade systems with different magnetic shear, and the high cadence and complete coverage of the *TRACE* 1600 Å Michelson Doppler Imager (MDI) magnetogram and *RHESSI* HXR observations. We pay particular attention to the electric field characteristics in different flare phases, as well as the temporal correlation with the HXR emission and its power-law spectral index and the photospheric magnetic field strength. We found that in the early impulsive phase, the reconnection electric field peaks just before the HXR emission peaks and the energy spectrum hardens. The result is consistent with the scenario that more particles are accelerated to higher energies by larger reconnection electric fields and then precipitate into the lower chromosphere to produce stronger HXR emissions. Such a particle acceleration mechanism plays its most significant role in the impulsive phase of this flare. In addition, our results provide evidence that the highly sheared magnetic field lines are mapped to the magnetic reconnection diffusion region to produce a large reconnection electric field.

Key words: Sun: flares – Sun: X-rays, gamma rays

1. INTRODUCTION

Magnetic reconnection in the corona is generally believed to be responsible for the particle acceleration and energy release in solar flares. Based on the two-dimensional CSHKP model (Carmichael 1964; Sturrock 1966; Hirayama 1974; Kopp & Pneuman 1976), the coronal magnetic field lines reconnect successively at higher and higher altitudes as the flare proceeds, which results in the formation of larger flare loops and further separation of two ribbons, as seen in Hα/UV images in the chromosphere. The energetic electrons accelerated via the reconnection electric field would precipitate into the chromosphere along magnetic loops and collide with the ambient plasma by thick-target bremsstrahlung (Dennis 1988) to produce hard X-ray (HXR) emission. Such HXR brightening sources most often appear as kernels at the outer edges of Hα/UV ribbons and are regarded as the footpoints of newly reconnected magnetic field lines. Since the coronal reconnection process cannot be observed directly, observations of chromospheric Hα/UV ribbons and HXR kernels, as well as photospheric magnetic fields, have been used to estimate the magnetic reconnection and energy release rates indirectly in many previous flare studies (e.g., Qiu et al. 2002, 2004, 2005; Wang et al. 2003; Asai et al. 2004; Jing et al. 2005, 2007; Krucker et al. 2005; Lee et al. 2006; Liu et al. 2008; Miklenic et al. 2007; Temmer et al. 2007).

According to the simplified 2.5-dimensional reconnection model, the rate of magnetic flux change per unit length along the X-line in the reconnecting current sheet is equal to the reconnection electric field. The magnetic flux change at the X-line is due to magnetic field lines entering the diffusion region to reconnect at the X-line. If we assume that electrons are accelerated by the reconnection electric field and move along the newly reconnected field lines down to the chromosphere to produce flare HXR kernels and Hα/UV ribbons, then the change of magnetic flux at the X-line can be obtained from the photospheric magnetic field flux swept by the outer edges of the flare ribbons (Choe & Cheng 2000; Forbes & Lin 2000). Simplifications have been made by many authors to calculate the flux change rate at the X-line from the product of the ribbon separation speed and the normal component of the photospheric magnetic field by assuming that the photospheric magnetic field does not change during the flaring process (Forbes & Priest 1984), or by assuming linear proportionality of magnetic fields from the photosphere to the corona and a constant area of the current sheet during a flare (Isobe et al. 2002; Asai et al. 2004).

The arcade magnetic field reconnection model predicts that HXR kernels, rather than Hα/UV ribbons, are positions where accelerated electrons release their energy via the thick-target bremsstrahlung process. Recent studies attempted to distinguish the magnetic reconnection and energy release conditions at the sites where the Hα ribbons coincide with and without HXR kernels (Asai et al. 2002, 2004; Miklenic et al. 2007; Temmer et al. 2007). They found that both the reconnection and energy release rates are stronger at the ribbon segments accompanied by HXR kernels than at those without HXR sources. Furthermore, because the HXR intensity correlates with the total energy of accelerated electrons and is thought to be proportional to the energy release rate in a flare (e.g., Hudson 1991), the correlation between the time variations of HXR intensity and

[6] Now at Physics Department, University of Alaska Fairbanks, AK 99775–5920, USA.

the magnetic reconnection rate (and the reconnection electric field) was expected, especially for the impulsive enhancement of HXR emission (Cheng et al. 2003). These temporal correlations have been verified subsequently by Qiu et al. (2004) and Jing et al. (2005) from Hα two-ribbon flares. In addition, the spatial variation of the reconnection rate associated with magnetic field lines in the ribbon-like HXR structure is noted, even though such a structure was rarely observed and only one *Yohkoh* event (the X5.7 flare on 2000 July 14 by Masuda et al. 2001) and one *Reuven Ramaty High Energy Solar Spectroscopic Imager* (*RHESSI*; Lin et al. 2002) event (the M8.0 flare on 2005 May 13 by Liu et al. 2007a) were reported. Jing et al. (2007) investigated the spatial distribution of HXR intensity along the ribbon-like HXR structure of the 2005 May 13 M8.0 flare and compared it with the magnetic reconnection rate and energy release rate derived from Hα and Michelson Doppler Imager (MDI) magnetic field measurements at the corresponding positions. They found that when the HXR sources appear as kernels, HXR intensity and the rates of magnetic reconnection and energy release have good spatial correlation. However, such a correlation is reduced as the HXR sources evolve to ribbon-like structures.

Recently, more *RHESSI* observations show that the HXR kernels in large flares display more complex motion patterns than the two-dimensional CSHKP model picture (e.g., Fletcher & Hudson 2002; Krucker et al. 2003; Bogachev et al. 2005; Grigis & Benz 2005; Yang et al. 2009). For example, the conjugate HXR kernels in the impulsive phase move mainly parallel or anti-parallel to the magnetic polarity inversion line and then perpendicularly. Since the movements of HXR conjugate footpoints represent the chromospheric footprints of newly reconnected magnetic field lines, different motion patterns could represent that reconnection occurred in different arcade magnetic fields.

Based on the complete coverage of the high-cadence *Transition Region and Coronal Explorer* (*TRACE*) 1600 Å, MDI magnetogram, and *RHESSI* HXR observations, the X10 flare on 2003 October 29 is selected in this study to investigate the temporal and spatial variations of the reconnection electric field due to its distinct two-phase HXR kernel motion and two arcade systems with different magnetic shear. The flare erupted from AR 10486 (S15W02) starting at 20:37 UT and reached a maximum of *Geostationary Operational Environmental Satellites* (*GOES*) soft X-ray (SXR) flux at 20:49 UT. It was a white-light (WL) flare first observed in the near-infrared continuum at 1.56 μm showing two ribbon separations (Xu et al. 2004). Strong HXR (Krucker et al. 2005) and γ-ray (Hurford et al. 2006) emissions were also observed by *RHESSI*. Prior to the flare, strong photospheric shear flows parallel to the magnetic neutral line (Yang et al. 2004), as well as increased current helicity density, were found in AR 10486 (Liu et al. 2007b); these are the signatures of magnetic shear increase and energy buildup in the pre-flare phase. Metcalf et al. (2005) proposed that there was an unusually large amount of magnetic free energy ($\sim 6\times10^{33}$ erg) in AR 10486 around the X10 flare's peak time. The significant reduction of current helicity density after the flare could be indicative of the untwisting magnetic flux loops (Liu et al. 2007b). Moreover, the converging motions of the *RHESSI* HXR kernels in the early phase and the diverging motion in the late phase were observed in this flare (e.g., Ji et al. 2008; Liu et al. 2009). This two-phase motion pattern of HXR kernels and the magnetic shear evolution can be interpreted by the magnetic reconnection taking place progressively from the inner, highly sheared arcade fields to the outer, weakly sheared arcade field lines (Yang et al. 2009). Therefore, it is reasonable to suppose that the reconnection electric field could have different properties in the impulsive and gradual phases of this flare.

Motivated by the two-phase magnetic reconnection process, the purpose of this paper is to characterize the evolution of the reconnection electric field in different flare phases. Two methods are used to estimate the reconnection electric field. One method is to calculate the change rate of photospheric magnetic flux in the newly brightened areas of *TRACE* UV ribbons, and the other is to calculate the product of HXR kernel motion speed and the corresponding photospheric magnetic field strength. We found that the enhancement of the reconnection electric field in the impulsive phase occurs before the increase in HXR kernel emission and the hardness of the energy spectrum. Our result is consistent with the scenario that more particles are accelerated to higher energies by larger reconnection electric fields and then precipitate into the lower chromosphere to produce stronger HXR emissions, even after the reconnection electric field peaks. In Section 2 we introduce the theory and formulas used for electric field estimation. The observational data and the analytical method are described in Section 3. The results are presented in Section 4. Discussions and conclusions are given in Sections 5 and 6, respectively.

2. THEORY

To involve the three-dimensional configurations of magnetic fields in reconnection and to avoid the errors due to two-dimensional model assumptions, we start from Faraday's law:

$$\nabla \times \vec{E} = -\frac{\partial \vec{B}}{\partial t}. \quad (1)$$

The electric field can be represented in terms of the magnetic flux ϕ as

$$\oint \vec{E} \cdot d\vec{l} = -\frac{\partial}{\partial t} \int \vec{B} \cdot d\vec{a} = -\frac{\partial \phi}{\partial t}. \quad (2)$$

In the solar atmosphere, since the magnetic flux is conserved along a field line from the photosphere to the corona, except at the reconnection X-point, the magnetic flux that participated in reconnection at the X-point can be calculated from the photospheric magnetic flux. Therefore, in two-ribbon flares, where the ribbon length is much larger than its width, the magnitude of the reconnection electric field E along the reconnecting current sheet can be inferred from the change rate of photospheric magnetic flux as follows:

$$El = \frac{\partial}{\partial t} \left(\int \vec{B} \cdot d\vec{a} \right), \quad (3)$$

where l indicates the length of the reconnecting current sheet, which can be regarded as the characteristic length of the energy release region or particle acceleration region along the reconnecting current sheet; and $d\vec{a}$ is the area segment of newly reconnected field lines in the photosphere. By assuming that the length of the reconnecting current sheet is the same as the ribbon length, the rate of photospheric magnetic flux change in newly reconnected field lines per unit length along the ribbon is equal to the reconnection electric field in the reconnecting current sheet (Forbes & Lin 2000). In this study, the newly brightened areas of *TRACE* UV ribbons are taken as the regions of newly

reconnected magnetic field lines. The magnetic flux change is thus only calculated at the image pixel i when its UV emission is increased after a time increment Δt. Namely, the magnetic flux change $\Delta\phi$ during a time interval Δt is $\Delta\phi = \sum_{i=1}^{n} B_{Ni} a_i$, where a_i is the area of the ith newly brightened pixel and B_{Ni} is the normal component of photospheric magnetic field strength at the corresponding position. The average reconnection electric field along the reconnection current sheet then can be estimated by

$$E = \frac{\sum_{i=1}^{n} B_{Ni} a_i}{L \Delta t}, \quad (4)$$

where L is the length of newly brightened areas along the ribbon.

Note that the UV ribbons and HXR kernels appeared simultaneously in the studied X10 flare, which represents the existence of a long reconnecting current sheet in the corona, with strong reconnection rates at local sites where magnetic field lines have strong HXR emissions at the chromospheric footpoints. Therefore, due to the kernel morphology of the HXR source and its small occupied area, the HXR kernel can be taken as a point, and the associated reconnection electric field can be further simplified from Equation (3) to the following form by assuming the magnetic field is independent of time:

$$E \cong \frac{B_N}{l} \frac{\partial a}{\partial t} \cong B_N V, \quad (5)$$

where B_N is the approximate normal magnetic field strength in the HXR kernel during the time increment when the HXR kernel is moving, and V is the average velocity of HXR kernel motion.

3. OBSERVATION AND DATA REDUCTION

3.1. TRACE UV Ribbons

TRACE provides high-cadence (less than 1 minute) and high-resolution (0.″5) observations of the 2003 October 29 X10 flare in the 1600 Å wavelength before 20:51 UT, which are useful in tracing the ribbon evolution in the evaluation of the reconnection electric field. As illustrated in Figure 1, multiple ribbons (black curves) were observed during the X10 flare, where the eastern and western ribbons appeared at ∼20:37 UT and the northern ribbon was first observed at ∼20:41 UT. By co-aligning with an MDI magnetogram in Figure 1(b), the eastern ribbon was located on the negative magnetic polarity side, while the western and northern ribbons were located on the positive magnetic polarity side. Those ribbons could be grouped into two sets of two-ribbon structure based on the flare loop morphology seen in *TRACE* 195 Å images, as shown in Figure 1(c). The magnetic fields in the northern ribbon would connect to the northern part of the eastern ribbon and those in the western ribbon would connect to the southern part of the eastern ribbon. Both two-ribbon structures expanded progressively as the flare proceeded.

The newly brightened areas in the *TRACE* ribbons are identified from a series of running-difference images. The intensities of all analyzed *TRACE* 1600 Å images are first linearly normalized to a quiescent region whose mean intensity was almost invariant before, during, and after the flare. The ribbon is identified when the normalized intensity is larger than 90% of the maximum in each image. However, some pixels, especially at locations coinciding with HXR kernels, are affected by the flare-produced energetic particles and thus have unreliable intensities. To minimize such errors in the further identification of newly brightened areas, the intensity at the

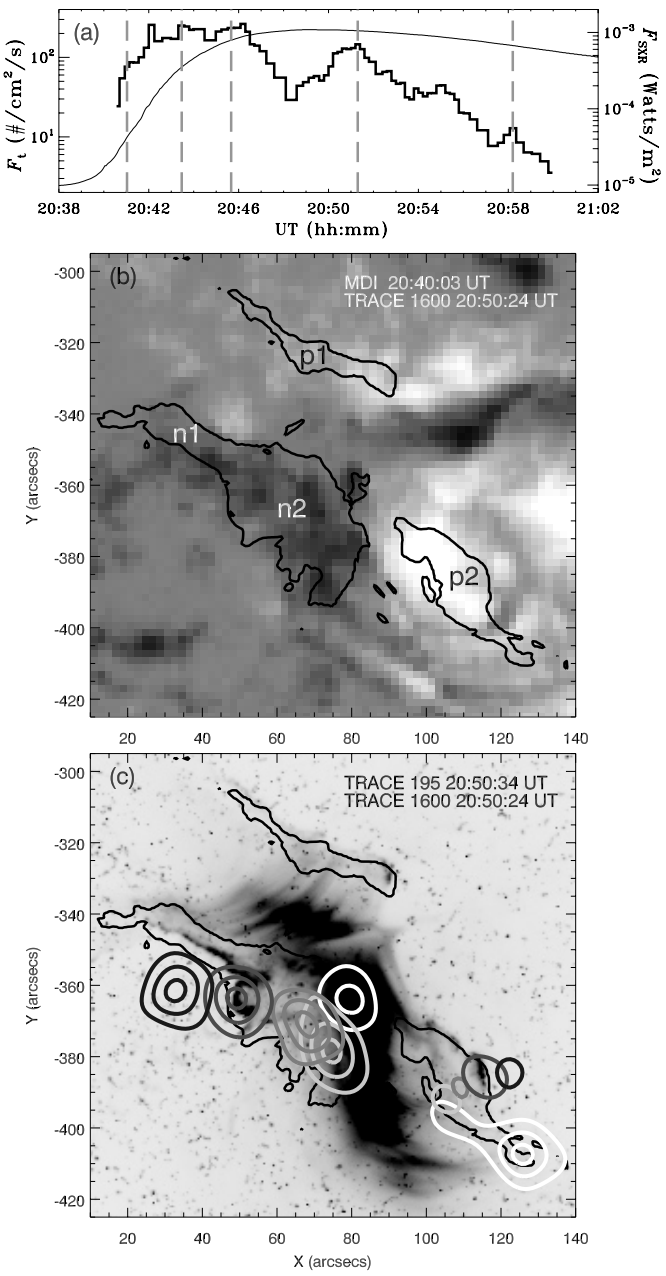

Figure 1. Illustration of arcade loop structures, multiple ribbons, and HXR kernel motions in the 2003 October 29 X10 flare. (a) Light curves of the *GOES* 1–8 Å flux (curve) and total HXR flux (histogram) in 50–100 keV in both HXR kernels. The dashed lines denote the times of the HXR sources shown in panel (c). (b) An MDI magnetogram superposed by *TRACE* 1600 Å ribbons (black curves). (c) Snapshot of the *TRACE* 195 Å image (inverse color) overlaid by *TRACE* 1600 Å ribbons (black curves) and HXR source positions at five specific times (gray contours from white to dark colors). The contour levels are 30%, 60%, and 90% of the maximum HXR emission in each *RHESSI* CLEAN map.

"contaminated" pixel is modified by the average of normalized intensities in the previous and proceeding images. Subsequently, the pixel is defined as newly brightened when the difference of modified intensities in adjacent images is larger than 10% of the maximum and located inside the studied ribbons. The selected newly brightened areas are then grouped into four divisions named n1, n2, p1, and p2, as marked in Figure 1(b), where the characters "n" and "p" represent the areas located at the negative and positive magnetic polarities, and the numbers "1" and "2" represent the northern and southern sets of

two-ribbon structure, respectively. The characteristic length L in each division is computed individually along the outmost edge of newly brightened areas. Note that the divisions of n2 and p2 are co-spatial with the HXR kernels, while n1 and p1 are located outside the HXR sources.

3.2. RHESSI HXR Kernels

The HXR images of this X10 flare are reconstructed from the *RHESSI* measurements in the energy band of 50–100 keV using the CLEAN algorithm (Hurford et al. 2002) with grids 3–6 (∼10" full-width half-maximum). The integration time for each image is set to be several times of the *RHESSI* rotation period (i.e., ∼4 s) varying from 8 s to 24 s such that at least one HXR source can be identified clearly in each CLEAN map. The periods shorter than 20 s after an attenuator change are excluded in the image reconstruction to eliminate the artificiality in the CLEAN maps. The HXR sources were first observed clearly at 20:40:34 UT, but multiple HXR kernels were found to be brightening alternately in the western ribbon before 20:43:20 UT. Note that the western HXR kernel is much weaker than the eastern one. To avoid identifying the noises in CLEAN maps, different localized regions with different criteria were used to obtain the quantities associated with HXR sources. A box enclosing each HXR kernel is first selected, and the region larger than 50% (80%) of the local maximum within the selected box is then used to determine the centroid position, the integrated HXR flux, and the corresponding photospheric magnetic field strength of the eastern (western) HXR source.

The positions of HXR sources at five specific times are indicated in Figure 1(c) by the gray contours, from white to dark colors, to display their motion patterns. The eastern kernel shows systematically southward motion in the impulsive phase, while both the eastern and western kernels move away from the magnetic polarity inversion line in the nearly perpendicular direction in the later period. Such a two-phase motion pattern of HXR kernels would be indicative of the two-phase magnetic reconnection process, which means the reconnection electric field could have different properties in the impulsive and gradual phases of this flare. The light curves of the *GOES* 1–8 Å flux (curve) and integrated HXR flux F_t (histogram) in the 50–100 keV range in both HXR kernels are shown in Figure 1(a), where the dashed lines denote the times of the HXR sources in Figure 1(c).

3.3. MDI Magnetogram

A time series of MDI magnetograms is used to determine the photospheric magnetic field strength beneath the newly brightened areas of *TRACE* 1600 Å ribbons. Because the flare was located close to the solar disk center, the line-of-sight magnetic field can be treated as the component normal to the local photospheric surface. Note that the MDI magnetic field measurement can be affected by flare-produced non-thermal electrons (Qiu & Gary 2003), resulting in magnetic anomaly features in the magnetograms during a flare. Such anomalies are characterized by the sudden reduction of magnetic field strength in positions co-spatial with HXR kernels. To discover the "contaminated" magnetograms, the total magnetic flux in the strong field region (i.e., field strength larger than 500 G) in AR 10486 is estimated and displayed in Figure 2(a). The quantities measured in the positive and negative magnetic polarities are indicated by the subscripts "p" and "n" and represented by the thick and thin curves, respectively. One

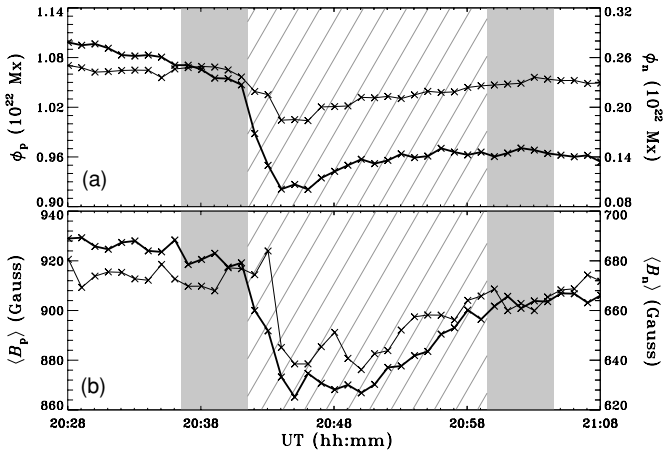

Figure 2. Time variations of (a) total magnetic flux and (b) average magnetic field strength in the strong magnetic field regions in AR 10486. The quantities measured from the positive (ϕ_p and $\langle B_p \rangle$) and negative (ϕ_n and $\langle B_n \rangle$) magnetic polarities are indicated by the thick and thin curves, respectively. The MDI magnetograms used for the reconnection electric field calculations are denoted by the vertical gray areas, while the "contaminated" magnetograms removed from the analysis are denoted by the vertical hatched area.

can see that the total magnetic fluxes in both polarities started to drop suddenly at 20:41 UT and did not recover to pre-flare states. A similar tendency is also found in the average magnetic field strength shown in Figure 2(b). The stop time of magnetogram contamination in this study is defined as the time when both magnetic flux and mean field strength become stable. Consequently, the magnetograms during 20:41:30–20:59:30 UT (vertical hatched area) are regarded to be "contaminated" and cannot be used for analysis.

Therefore, for the electric field calculation during the contamination period, 10 temporary $\Delta\phi$ values corresponding to the newly brightened areas are first derived from the five magnetograms before 20:41:30 UT and the five magnetograms after 20:59:30 UT, as denoted by the first and second vertical gray areas in Figure 2. The final $\Delta\phi$ at a certain time together with its lower and upper bounds are then obtained from the average, minimum, and maximum of these 10 temporary $\Delta\phi$ values, respectively. The same procedures are applied to the period before 20:41:30 UT (after 20:59:30 UT), but only five temporary $\Delta\phi$ values derived from the corresponding five magnetograms are used for the calculations. Each magnetogram is differentially rotated to the times of *TRACE* running-difference images before analysis.

3.4. Alignment

The *TRACE* 1600 Å and *RHESSI* HXR images are aligned to the MDI magnetograms separately. The *RHESSI* HXR images are aligned to the MDI magnetograms by finding the spatial coincidence between HXR kernels and MDI magnetic anomaly features. The *TRACE* 1600 Å images are aligned to the MDI magnetograms by matching the sunspot features in the *TRACE* WL and the MDI continuum images. If the corresponding *TRACE* WL images are unavailable, the *TRACE* 1600 Å images are first aligned to the *RHESSI* HXR images by spatially correlating the saturated features in the 1600 Å ribbons with the HXR kernels. Subsequently, the alignment between the *TRACE* 1600 Å images and the MDI magnetograms is obtained by aligning the *RHESSI* HXR images with the MDI magnetograms.

3.5. Electric Field Calculation

For *TRACE* 1600 Å observations, the reconnection electric field in each division E_j is evaluated individually by Equation (4), where the subscript *j* indicates the quantities measured in a specific ribbon division (i.e., n1, n2, p1, and p2). The reconnection electric fields for the northern and southern sets of two-ribbon structure are obtained separately by $E_1 = (E_{n1} + E_{p1})/2$ and $E_2 = (E_{n2} + E_{p2})/2$. For *RHESSI* HXR observations, it is inappropriate to estimate the reconnection electric field via the running-difference image. The shape of the *RHESSI* HXR kernel in reality is narrower than that appearing in the CLEAN map due to the application of a position function in the image reconstruction. Pinpointing the newly brightened areas in the HXR running-difference image is meaningless because of the large uncertainty. Therefore, the reconnection electric field associated with HXR kernels is obtained from the product of the HXR kernel velocity and the photospheric magnetic field strength, as given in Equation (5).

The uncertainties in the electric field calculation in this study come from the following aspects. (1) Identification of newly brightened areas: the threshold of the 10% maximum of the renormalized brightness in UV running-difference images was chosen because more brightened pixels can be identified in the studied ribbons. (2) Magnetic field approximation: since UV ribbons and HXR footpoints are the chromospheric features, it is more reasonable to calculate the electric field from the chromospheric magnetic field instead of the photospheric magnetic field. In general, the magnetic field strength decreases with height above an active region (Leka & Metcalf 2003). The usage of the photospheric magnetic field in the calculation would slightly overestimate the electric field because of the small thickness (∼1000 km) of the chromosphere. Moreover, the image co-alignment between different instruments would also produce uncertainty in the measurement of magnetic field strength. (3) HXR kernel velocity estimation: the complex morphology of the HXR source or the weak HXR emission would make it difficult to pinpoint the HXR source and thus produce uncertainty in the velocity estimation.

4. RESULTS

4.1. Reconnection Electric Field from UV Ribbons

Time variation of the reconnection electric field E_2 obtained from the southern two-ribbon structure is shown as the black histogram in Figure 3(a). The integrated HXR flux F_t in the 50–100 keV range at the conjugate HXR footpoints is indicated by the gray histogram. It is obvious that in the early impulsive phase, the reconnection electric field peaks (∼2.7 kV m^{-1} at 20:40:43 UT) prior to the HXR flux enhancement. However, such a feature cannot be found after 20:49 UT. We also estimated the electric field E_1 from the northern two-ribbon set, and the result is shown in Figure 3(b) for comparison. One can see that E_1 has similar time variation than E_2 but has smaller magnitude with the maximum of ∼1.2 kV m^{-1} at 20:41:53 UT. This indicates that a larger electric field is found in the arcade areas accompanying HXR kernels than in areas without HXR kernels. Moreover, according to the post-flare loops seen in *TRACE* 195 Å images, the arcade magnetic field lines in the southern two-ribbon set are much more sheared than those in the northern set, which implies that the reconnection electric field in the highly sheared arcade fields is larger than that in the weakly sheared arcade fields.

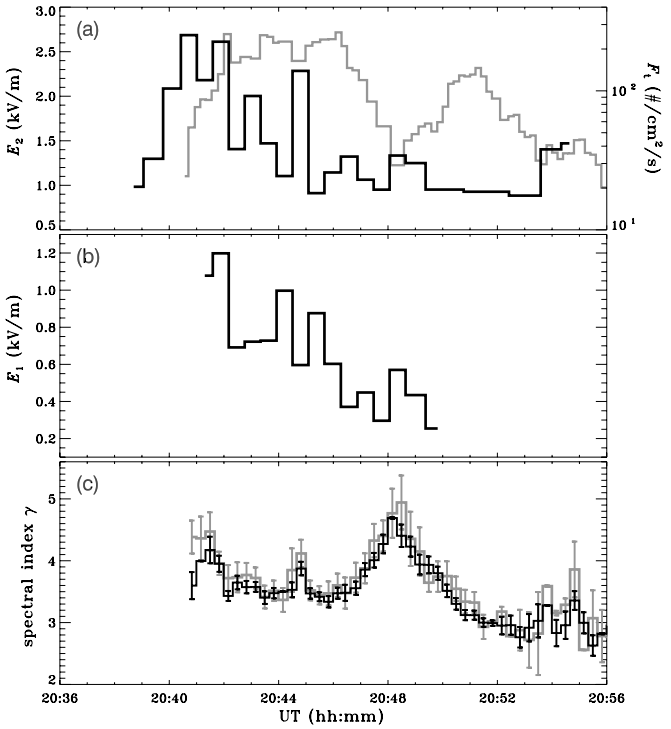

Figure 3. Time variations of the reconnection electric fields obtained from the (a) southern and (b) northern two-ribbon structures. The total HXR footpoint flux (gray histogram) in the 50–100 keV range is also shown in panel (a) for comparison. (c) Time variations of the HXR spectral index in the eastern (black histogram) and western (gray histogram) footpoints, obtained from Liu et al. (2009).

On the other hand, the spectrum of X-ray emission is a useful diagnostic to understand the significance of the reconnection electric field in accelerating non-thermal electrons in solar flares. The harder X-ray spectrum, which is represented by the smaller value of power-law spectral index γ, means more electrons are accelerated to higher energies before impinging on the chromosphere and are thought to be associated with a larger electric field in the reconnecting current sheet in the corona. Thus, it is worthwhile to discuss the relationship between the reconnection electric field and the X-ray emission spectral index. Figure 3(c) shows the time variation of the power-law spectral index in individual HXR kernels of the X10 flare analyzed by Liu et al. (2009), where the black (gray) histogram represents the eastern (western) kernel. We found that in the early impulsive phase, the spectral index γ starts to decrease (i.e., the spectrum becomes harder) as the reconnection electric field peaks. Such a feature is consistent with the scenario that highly sheared field lines have more magnetic free energy to release via magnetic reconnection in the corona, and the enhancement of the reconnection electric field in the early impulsive phase can accelerate more non-thermal electrons to higher energies. More energetic electrons can thus precipitate into the lower chromosphere to produce stronger HXR emissions.

To characterize the magnetic fluxes joined in reconnection from opposite magnetic polarities, the reconnection electric field (black histogram) from each ribbon division and the ratio of reconnection flux from negative and positive magnetic polarities are estimated individually, as shown in Figure 4, where the solid (empty) square in Figure 4(e) denotes the reconnection flux ratio $R_{\phi 2}$ ($R_{\phi 1}$) measured from the southern (northern) two-ribbon structure. The integrated HXR fluxes at the eastern

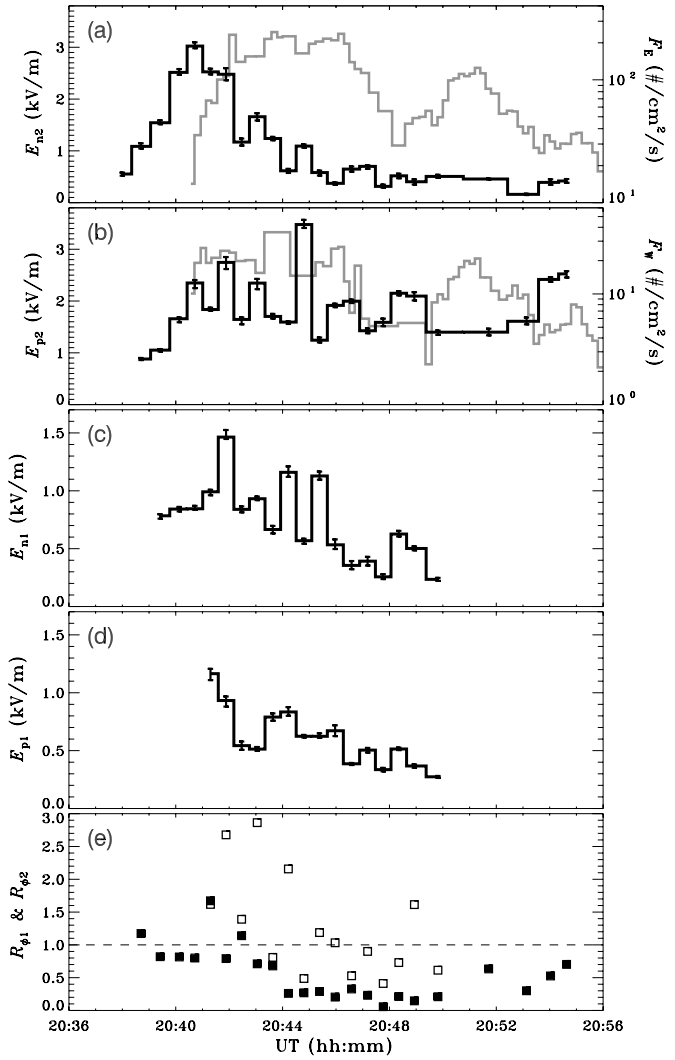

Figure 4. Time variations of the reconnection electric fields (black histograms) obtained from the divisions of (a) n2, (b) p2, (c) n1, and (d) p1. The integrated HXR fluxes at the eastern and western footpoints are indicated by the gray histograms in panels (a) and (b), respectively. (e) Time variation of the reconnection flux ratio measured in the northern (empty square) and southern (solid square) two-ribbon structures.

and western HXR footpoints, F_E and F_W, are indicated by the gray histograms in Figures 4(a) and (b) for comparison. They clearly show that E_{n2} has more systematic variation than E_{p2} during the entire flare period, and E_{n2} increases monotonously in the early phase, reaches a maximum value of $\sim 3\,\mathrm{kV\,m^{-1}}$ at 20:40:43 UT, and then decreases gradually in the late phase. In particular, E_{n2} is found to peak $\sim$1 minute prior to the peak of F_{n2} in the early phase. Both E_{n1} and E_{p1} decrease gradually in a similar manner. As shown in Figure 4(e), the reconnection fluxes between positive and negative polarities are in general different during most of the flaring period and thus result in the difference between E_{n2} (E_{n1}) and E_{p2} (E_{p1}). In principle, the reconnection fluxes from opposite magnetic polarities should be identical. Such a difference could come from inaccurate measurements, such as the remote connection of magnetic field lines, or the identification of newly brightened areas and HXR kernels.

4.2. The Reconnection Electric Field from HXR Kernels

On the other hand, we also estimate the reconnection electric field from HXR kernel motions to independently examine the magnitude of the electric field via different observations and methods. Figure 5(a) shows the distances between two conjugate HXR kernels, whose positions are determined from the two-dimensional elliptical Gaussian fitting of HXR kernels, in the perpendicular ($D_\perp$, cross signs) and parallel ($D_{//}$, plus signs) directions with respect to the magnetic polarity inversion line. The corresponding velocities $V_\perp$ and $V_{//}$ are obtained from the time variations of $D_\perp$ and $D_{//}$ respectively via a linear fitting, as denoted by the straight black lines. The light curve of the total HXR flux in conjugate footpoints (F_t) in the 50–100 keV range is also shown as a histogram for comparison. To trace the electric field evolution, linear fits are applied separately in five different periods and thus five values of $V = \sqrt{V_\perp^2 + V_{//}^2}$ are derived. Period I (20:40:34–20:41:26 UT) is in the early impulsive phase, which corresponds to the period before the first peak of F_t. Period II (20:41:54–20:42:48 UT) is also in the early impulsive phase but occurs during the first peak of F_t. Period III (20:45:06–20:47:24 UT) is in the late impulsive phase corresponding to the third peak of F_t. Period IV (20:49:14–20:51:54 UT) is in the main phase and corresponds to the fourth peak of F_t. Period V (20:52:18–20:59:58 UT) is in the gradual decay phase. Figure 5(b) shows the time variations of the mean magnetic field strengths in the photosphere at the eastern (B_E, black cross signs) and western (B_W, gray cross signs) HXR kernels. The magnetic field strength B at a certain time is derived by $(B_E+B_W)/2$. The B_N value used for electric field calculation in Equation (5) together with its lower and upper bounds are then obtained from the average, minimum, and maximum of B in each defined period. The reconnection electric field is estimated by VB_N.

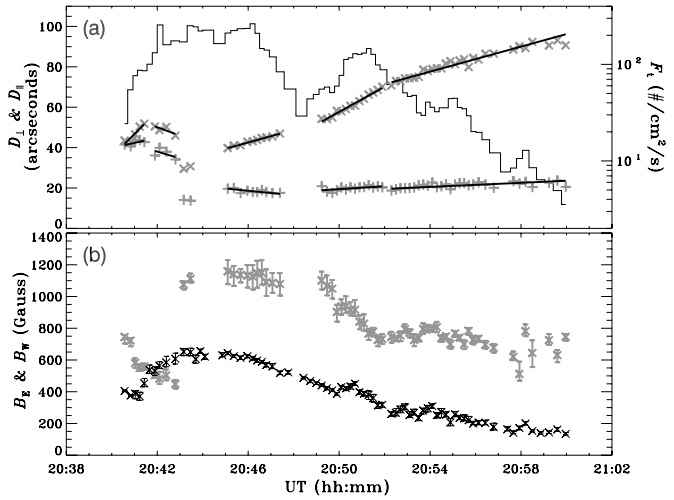

Figure 5. (a) Time variations of the perpendicular (cross signs) and parallel (plus signs) components of the distance between two HXR kernels. The velocity obtained from the time deviation of the displacement via a linear fitting is indicated by a straight line. The light curve of total HXR flux in both footpoints is denoted by the histogram. (b) Time variations of the photospheric magnetic field strengths in the eastern (black cross sign) and western (gray cross sign) HXR kernels.

To understand the data shown in Figure 5, we summarize in Table 1 the HXR kernel speed (from Columns 2 to 4), the magnetic field strength in the HXR kernels (from Columns 5 to 7), and the computed reconnection electric field (from Columns 8 to 10), where the fitting period is given in the first column. It is found that the primary peak of the reconnection electric field occurs in Period I, when HXR emission starts

Table 1
Physical Quantities Obtained from Two HXR Footpoints

Period	Speed (km s^{-1})			Magnetic Field (G)			Electric Field (kV m^{-1})		
	$V_\perp$	$V_{//}$	V	$\langle B\rangle$	$B_{\rm min}$	$B_{\rm max}$	E	$E_{\rm min}$	$E_{\rm max}$
I (20:40:34–20:41:26)	134.49	30.18	137.83	515.12	460.77	575.18	7.10	6.35	7.93
II (20:41:54–20:42:48)	50.91	40.89	65.30	519.55	506.35	533.89	3.39	3.31	3.49
III (20:45:06–20:47:24)	37.62	13.44	39.95	859.68	798.49	901.43	3.43	3.19	3.60
IV (20:49:14–20:51:54)	75.27	8.56	75.75	644.81	520.08	771.02	4.88	3.94	5.84
V (20:52:18–20:59:58)	37.44	6.15	37.94	445.57	413.01	484.28	1.69	1.57	1.84

Table 2
Summary of the Reconnection Electric Field Calculation for the 2003 October 29 X10 Flare in Different Studies

Studies	Peak E (kV m^{-1})	Formula	Instrument
Xu et al. (2004)	4.5	$V B_N$	Near-infrared
Jing et al. (2005)	3.8	$V B_N$	Hα
Krucker et al. (2005)	6.7	$V B_N$	*RHESSI* HXR
Liu & Wang (2009)	1.7	$\frac{\langle\dot{\phi}\rangle}{\langle L\rangle}$	Hα
This Study	7.1	$V B_N$	*RHESSI* HXR
This Study	2.7	$\frac{1}{L}\frac{\partial\phi}{\partial t}$	*TRACE* UV

to increase in the early impulsive phase. The secondary peak of the reconnection electric field is found in Period IV, when two conjugate HXR kernels start to separate systematically in the perpendicular direction. Note that the reconnection electric fields derived from UV ribbon and HXR kernel observations peak mainly in Period I, while the secondary peak of the electric field occurs in different flare periods in UV ribbon and HXR kernel observations.

5. DISCUSSION

The reconnection electric field of the 2003 October 29 X10 flare has been investigated in previous studies. Table 2 summarizes the comparison of the peak electric field in this X10 flare. One can see that by using *RHESSI* HXR observations, our maximum electric field of 7.1 kV m^{-1} is similar to the 6.7 kV m^{-1} obtained by Krucker et al. (2005). We also found that the electric field derived from Equation (5) has a larger maximum value than the electric field derived from Equation (4). On the other hand, the velocity of HXR kernel motion is calculated at a certain position because of its kernel morphology, which is different from the average velocity used in Hα and near-infrared ribbon expansions. This results in larger values of the peak electric field in HXR kernel observations.

Liu & Wang (2009) investigated the correlation between the maximum reconnection electric field and the minimum γ value in 13 two-ribbon flares, including the 2003 October 29 X10 flare. They found that a flare with larger magnitude corresponds to a larger reconnection electric field and a harder HXR spectrum. In their study, the quantities of this X10 flare event were only obtained from the later phase when two ribbons separated progressively. Their electric field is estimated from the magnetic flux change rate divided by a constant L, where L represents the ribbon length when the ribbon is fully developed. However, the ribbon length changes with time in reality, especially in the impulsive phase. For the X10 flare, the eastern ribbon is observed to elongate southward before ~20:43 UT, which coincides with the parallel motion of the eastern HXR kernel, indicating rapid changes in ribbon length. Therefore, the time-dependent variation of the ribbon length in the direction parallel to the magnetic polarity inversion line, as suggested by Lee & Gary (2008), is taken into account in the reconnection electric field calculation in this study.

In addition, we also analyze the relationship between footpoint motion speed and local photospheric magnetic field strength at two conjugate HXR kernels. For each footpoint, the displacement from its first position is calculated and then decomposed to the perpendicular and parallel components with respect to the magnetic polarity inversion line to derive the velocities $V_\perp$ and $V_{//}$. Table 3 summarizes the footpoint motion speed $V = \sqrt{V_\perp^2 + V_{//}^2}$; the average photospheric magnetic field strength $\langle B\rangle$ in each defined period; the reconnection electric field $E = V\langle B\rangle$; and the local maximum HXR flux $F_{\rm max}$. The subscripts "E" and "W" in Table 3 represent the quantities measured from the eastern and western HXR kernels, respectively. Our results show that the motion speed of the eastern HXR kernel, which is located at the smaller magnetic field strength region, is faster than that of the western HXR kernel. Namely, HXR kernels move faster in weaker magnetic field regions. This behavior is consistent with previous studies (Jing et al. 2007, 2008; Lee & Gary 2008) that ribbon separation speed anti-correlates with the local magnetic field strength. On the other hand, we also compare the HXR kernel motion speed with the maximum of the local HXR flux. Although there is no clear temporal correlation between these two quantities, the fastest motion speed and the largest local maximum HXR flux are found to occur in the impulsive phase. This may indicate that in the early flare period, more coronal magnetic fields are carried into the diffusion region more rapidly to participate in reconnection, such that larger electric fields are produced in the

Table 3
Physical Quantities Obtained from the Eastern and Western HXR Footpoints Individually

Period	Speed (km s^{-1})		Magnetic Field (G)		Electric Field (kV m^{-1})		HXR Flux (counts cm^{-2} s^{-1})	
	$V_{\rm E}$	$V_{\rm W}$	$\langle B_{\rm E}\rangle$	$\langle B_{\rm W}\rangle$	$E_{\rm E}$	$E_{\rm W}$	$(F_{\rm E})_{\rm max}$	$(F_{\rm W})_{\rm max}$
I (20:40:34–20:41:26)	138.62	69.80	398.66	631.58	5.34	4,54	67.79	26.02
II (20:41:54–20:42:48)	75.32	73.38	554.14	484.97	4.17	3.76	232.54	24.54
III (20:45:06–20:47:24)	26.06	13.59	594.78	1124.58	1.58	1.53	236.88	26.61
IV (20:49:14–20:51:54)	43.93	33.29	396.59	893.02	1.79	3.06	125.19	20.90
V (20:52:18–20:59:58)	24.44	8.12	222.15	728.92	0.55	0.59	56.02	11.91

reconnecting current sheet and more HXR emissions are observed in the chromosphere. But the particle acceleration caused directly by the reconnection electric field becomes weak in the later period, implying that other acceleration mechanisms become important in the late phase.

Our results show that the reconnection electric fields derived from HXR and UV observations have different temporal variations, especially in the later flare phase and for the weaker HXR source. This discrepancy could come from different measurements using different instruments. The *TRACE* 1600 Å emission can be produced by the precipitation of non-thermal electrons and by the thermal conduction from the reconnected loops (Fletcher & Hudson 2002). The HXR kernel emission, however, is produced by the precipitation of accelerated electrons along newly reconnected field lines impinging on the chromosphere and is thought to map to the primary energy release site in the corona.

6. CONCLUSION

Based on the comprehensive coverage of high-resolution and high-cadence observations by MDI, *TRACE*, and *RHESSI* spacecraft, the 2003 October 29 X10 flare is selected here to investigate the reconnection electric field and its temporal and spatial correlations with HXR kernel emission and photospheric magnetic field strength. To estimate the arcade magnetic field reconnection rate via different measurements, the electric field in the reconnecting current sheet is inferred not only from the magnetic flux change rate in the newly brightened areas of *TRACE* 1600 Å ribbons, but also from the product of HXR kernel motion speed and the corresponding photospheric magnetic field strength.

In this study, the multiple ribbons observed in *TRACE* 1600 Å images are grouped into northern and southern sets of two-ribbon structure with four divisions (n1, p1, n2, and p2) to characterize the magnetic reconnection conditions in different arcade loops. The northern set (n1 and p1) has weakly sheared arcade magnetic field lines without any HXR source, while the southern set (n2 and p2) has highly sheared arcade field lines accompanying HXR sources at the footpoints. The derived electric field is found to be larger in the southern two-ribbon structure than in the northern two-ribbon structure. Note that in previous studies, the spatial correspondence of the HXR source to the reconnection electric field is analyzed by selecting several tracking paths across or along specific ribbons. Therefore, our result provides evidence, for the first time, that highly sheared arcade field lines produce larger reconnection electric fields than weakly sheared arcade field lines, and more HXR emissions are thus observed at the footpoints of highly sheared reconnected field lines.

By comparing the time variation of HXR emissions in both HXR kernels of this X10 flare, we found that the reconnection electric field in the early impulsive phase peaked prior to the increase in HXR flux and the decrease of the spectral index. We thus conclude that the reconnection electric field plays a key role in particle acceleration in the impulsive phase of a large flare, while other acceleration mechanisms could be important in later flare periods.

We are grateful to the *GOES*, *SOHO*, *TRACE*, and *RHESSI* teams for providing the datasets. The authors also thank Dr. Wei Liu for providing HXR spectral index information. This work is supported by the National Cheng Kung University and the National Science Council of R.O.C. under grant NSC 98–2111-M-006–001-MY3.

REFERENCES

Asai, A., Masuda, S., Yokoyama, T., Shimojo, M., Isobe, H., Kurokawa, H., & Shibata, K. 2002, ApJ, 578, L91
Asai, A., Yokoyama, T., Shimojo, M., Masuda, S., Kurokawa, H., & Shibata, K. 2004, ApJ, 611, 557
Bogachev, S. A., Somov, B. V., Kosugi, T., & Sakao, T. 2005, ApJ, 630, 561
Carmichael, H 1964, in The Physics of Solar Flares, ed. W. N. Hess (NASA SP-50; Washington, DC: NASA), 451
Cheng, C. Z., Ren, Y., Choe, G. S., & Moon, Y. J. 2003, ApJ, 596, 1341
Choe, G. S., & Cheng, C. Z. 2000, ApJ, 541, 449
Dennis, B. R. 1988, Sol. Phys., 118, 49
Fletcher, L., & Hudson, H. 2002, Sol. Phys., 210, 307
Forbes, T. G., & Lin, J. 2000, J. Atmos. Sol.-Terr. Phys., 62, 1499
Forbes, T. G., & Priest, E. R. 1984, in Solar Terrestrial Physics: Present and Future, ed. D. M. Butler & K. Papadopoulus (Washington DC: NASA), 1
Grigis, P. C., & Benz, A. O. 2005, ApJ, 625, L143
Hirayama, T. 1974, Sol. Phys., 34, 323
Hudson, H. S. 1991, Sol. Phys., 133, 357
Hurford, G. J., Krucker, S., Lin, R. P., Schwartz, R. A., Share, G. H., & Smith, D. M. 2006, ApJ, 644, L93
Hurford, G. J., et al. 2002, Sol. Phys., 210, 61
Isobe, H., Yokoyama, T., Shimojo, M., Morimoto, T., Kozu, H., Eto, S., Narukage, N., & Shibata, K. 2002, ApJ, 566, 528
Ji, H., Wang, H., Liu, C., & Dennis, B. R. 2008, ApJ, 680, 734
Jing, J., Chae, J., & Wang, H. 2008, ApJ, 672, L73
Jing, J., Lee, J., Liu, C., Gary, D. E., & Wang, H. 2007, ApJ, 664, L127
Jing, J., Qiu, J., Lin, J., Qu, M., Xu, Y., & Wang, H. 2005, ApJ, 620, 1085
Kopp, R. A., & Pneuman, G. W. 1976, Sol. Phys., 50, 85
Krucker, S., Fivian, M. D., & Lin, R. P. 2005, Adv. Space Res., 35, 1707
Krucker, S., Hurford, G. J., & Lin, R. P. 2003, ApJ, 595, L103
Lee, J., & Gary, D. E. 2008, ApJ, 685, L87
Lee, J., Gary, D. E., & Choe, G. S. 2006, ApJ, 647, 638
Leka, K. D., & Metcalf, T. R. 2003, Sol. Phys., 212, 361
Lin, R. P., et al. 2002, Sol. Phys., 210, 3
Liu, C., Lee, J., Gary, D. E., & Wang, H. 2007a, ApJ, 658, L127
Liu, C., Lee, J., Jing, J., Gary, D. E., & Wang, H. 2008, ApJ, 672, L69
Liu, C., & Wang, H. 2009, ApJ, 696, L27
Liu, W., Petrosian, V., Dennis, B. R., & Holman, G. D. 2009, ApJ, 693, 847
Liu, Y., Kurokawa, H., Liu, C., Brooks, D. H., Dun, J., Ishii, T. T., & Zhang, H. 2007b, Sol. Phys., 240, 253
Masuda, S., Kosugi, T., & Hudson, H. S. 2001, Sol. Phys., 204, 55
Metcalf, T. R., Leka, K. D., & Mickey, D. L. 2005, ApJ, 623, L53
Miklenic, C. H., Veronig, A. M., Vršnak, B., & Hanslmeier, A. 2007, A&A, 461, 697
Qiu, J., & Gary, D. E. 2003, ApJ, 599, 615
Qiu, J., Lee, J., Gary, D. E., & Wang, H. 2002, ApJ, 565, 1335
Qiu, J., Wang, H., Cheng, C. Z., & Gray, D. E. 2004, ApJ, 604, 900
Qiu, J., & Yurchyshyn, V. B. 2005, ApJ, 634, L121
Sturrock, P. A. 1966, Nature, 211, 695
Temmer, M., Veronig, A. M., Vršnak, B., & Miklenic, C. 2007, ApJ, 654, 665
Wang, H., Qiu, J., Jing, J., & Zhang, H. 2003, ApJ, 593, 564
Xu, Y., Cao, W., Liu, C., Yang, G., Qiu, J., Jing, J., Denker, C., & Wang, H. 2004, ApJ, 607, L131
Yang, G., Xu, Y., Cao, W., Wang, H., Denker, C., & Rimmele, T. R. 2004, ApJ, 617, L151
Yang, Y. H., Cheng, C. Z., Krucker, S., Lin, R. P., & Ip, W. H. 2009, ApJ, 693, 132